

Nucleosynthesis of an 11.8 M_{\odot} Supernova with 3D Simulation of the Inner Ejecta: Overall Yields and Implications for Short-Lived Radionuclides in the Early Solar System

A. SIEVERDING,¹ B. MÜLLER,² AND Y.-Z. QIAN¹

¹*School of Physics and Astronomy, University of Minnesota, Minneapolis, MN 55455, USA*

²*School of Physics and Astronomy, Monash University, Victoria 3800, Australia*

ABSTRACT

Based on a 3D supernova simulation of an 11.8 M_{\odot} progenitor model with initial solar composition, we study the nucleosynthesis using tracers covering the innermost 0.1 M_{\odot} of the ejecta. These ejecta are mostly proton-rich and contribute significant amounts of ^{45}Sc and ^{64}Zn . The production of heavier isotopes is sensitive to the electron fraction and hence the neutrino emission from the proto-neutron star. The yields of these isotopes are rather uncertain due to the approximate neutrino transport used in the simulation. In order to obtain the total yields for the whole supernova, we combine the results from the tracers with those for the outer layers from a suitable 1D model. Using the yields of short-lived radionuclides (SLRs), we explore the possibility that an 11.8 M_{\odot} supernova might have triggered the formation of the solar system and provided some of the SLRs measured in meteorites. In particular, we discuss two new scenarios that can account for at least the data on ^{41}Ca , ^{53}Mn , and ^{60}Fe without exceeding those on the other SLRs.

Keywords: core-collapse supernova, nucleosynthesis, massive stars

1. INTRODUCTION

Core-collapse supernovae (CCSNe), which mark the end of the lives of massive stars, are important sites for nucleosynthesis by producing most of the elements up to and including the Fe group (e.g., Nomoto et al. 2013; Thielemann et al. 1996). Parameterized models based on pistons or thermal energy injections in spherical symmetry have been widely used to guide our understanding of CCSN contributions to chemical enrichment of the universe (e.g., Woosley et al. 2002; Heger & Woosley 2010). Being computationally efficient, such models can be calibrated to well-known observables and then be employed to explore fine grids of initial mass, metallicity, and rotation (e.g., Limongi & Chieffi 2018). They, however, have proven inadequate for predicting the conditions of the inner CCSN ejecta and hence the associated nucleosynthesis (Wanajo et al. 2018; Harris et al. 2017; Lentz et al. 2015; Young & Fryer 2007). With an improved understanding of the CCSN mechanism (e.g., Lentz et al. 2015; Janka et al. 2016; Müller 2016; O'Connor & Couch 2018; Burrows et al. 2020), advanced parameterizations for explosions in spherical symmetry have been developed (Ebinger et al. 2019; Ertl et al. 2016). Yet it remains unclear whether such parameterizations can accurately predict the conditions of the ejecta directly affected by the dynamics of the neutrino-driven explosion. Fully self-consistent multi-D simulations are important benchmarks for such models.

An increasing number of 3D simulations have been performed recently (Burrows et al. 2020; Glas et al. 2018; Müller et al. 2019), but detailed studies of the nucleosynthesis so far have been based mostly on 2D models (Eichler et al. 2018; Wanajo et al. 2018; Harris et al. 2017). It has become clear, however, that there are systematic differences between the dynamics of 2D and 3D explosions (Müller 2015), which might affect the nucleosynthesis. Therefore, 3D simulations are required to address definitively the nucleosynthesis of the inner ejecta that are directly affected by the explosion mechanism, especially the production of the Fe-group and heavier elements. Reliable nucleosynthesis predictions require running 3D simulations until several seconds after core bounce, which, however, is not done in most cases due to the extremely high computational cost.

In this study, we calculate the nucleosynthesis of an 11.8 M_{\odot} CCSN based on a 3D simulation with the CoCoNuT-FMT code (Müller et al. 2019; Müller & Janka 2015). The simulation was run until ≈ 1.2 s after core bounce, long enough to cover most of the explosive nucleosynthesis for the whole Si shell and part of the O/Ne layer. Using 2D models, Wanajo et al. (2018) already pointed out differences in the yield pattern from such inner ejecta compared to commonly adopted parameterizations in spherical symmetry. For progenitors with similar masses to the one studied here, they found larger production factors of ^{45}Sc and ^{64}Zn because neutrino interaction results in a larger variability of the electron fraction Y_e in 2D. We confirm this finding for the first

time with a 3D model. Regarding the production of heavier isotopes, however, we find that to reach firm conclusions, our simulation must be improved by incorporating more accurate neutrino transport to determine self-consistently the Y_e of the neutrino-heated ejecta.

To obtain the total yields of the $11.8 M_\odot$ CCSN, we combine the results for the inner ejecta from the tracers with those for the outer layers from a suitable explosion model in spherical symmetry. Using the yields of short-lived radionuclides (SLRs, with lifetimes up to several 10^7 yr), we explore the possibility that such a CCSN might have triggered the formation of the solar system and provided some of the SLRs measured in meteorites. The $11.8 M_\odot$ progenitor model with initial solar composition is of special interest. Banerjee et al. (2016) showed that if a reasonably small amount of the inner material is allowed to fall back onto the proto-neutron star (PNS), the yields from a parameterized 1D explosion of this model are consistent with the meteoritic data and can account for the abundances of the SLRs ^{10}Be , ^{41}Ca , and ^{107}Pd in the early solar system (ESS). In contrast, typical CCSNe from more massive stars tend to grossly overproduce the SLRs ^{53}Mn and ^{60}Fe and cause large shifts in stable isotopes that are not observed. At the end of our 3D CCSN simulation, we find that the yields of ^{53}Mn and ^{60}Fe of the $11.8 M_\odot$ model are comparable to those obtained by Banerjee et al. (2016) without fallback. Because neither our 3D simulation nor our 1D model shows any indication of fallback, we discuss two new scenarios that can account for at least the ESS data on ^{41}Ca , ^{53}Mn , and ^{60}Fe without exceeding those on the other SLRs. Banerjee et al. (2016) also showed that ^{10}Be is commonly produced by CCSNe. We study the production of this SLR by the $11.8 M_\odot$ model in detail and identify several sources of uncertainty.

The plan of this paper is as follows. In §2 we discuss our method of extracting Lagrangian tracers from the 3D simulation and the setup for the nucleosynthesis calculations. In §3 we give an overview of the nucleosynthesis of the inner ejecta calculated with the tracers. In §4 we present the yields for the entire CCSN combining the results for the inner ejecta and those for the outer ejecta calculated with an appropriate 1D model. We also discuss the production of the SLR ^{10}Be in detail. In §5 we focus on the SLR yields and discuss their implications for the ESS. In §6 we summarize our results and give conclusions.

2. METHOD

The $11.8 M_\odot$ progenitor model is of the solar composition initially and was evolved with the 1D hydrodynamics code KEPLER (Weaver et al. 1978) by Banerjee et al. (2016) to explore candidates for a possible CCSN trigger for the formation of the solar system. Müller et al. (2019) carried out a 3D CCSN simulation based on this model. We refer readers

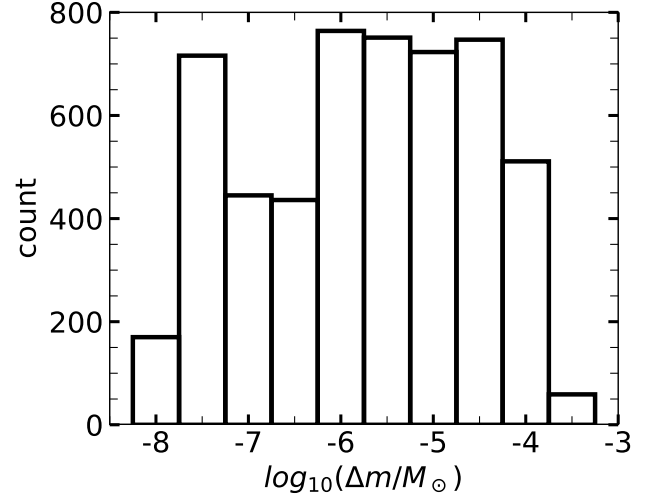


Figure 1. Histogram for the number of tracers as a function of their masses.

to that work for details of the simulation. We describe in this section how we extract the conditions of the inner ejecta from the simulation and how we calculate the nucleosynthesis of the CCSN.

2.1. Tracer Extraction

At the end of the 3D CCSN simulation, we place tracers on a spatial grid that is equally spaced in $\log_{10} r$, $\cos \theta$, and ϕ , where r is the radius ranging from 100 to 15,000 km, θ is the polar angle, and ϕ is the azimuthal angle. We assign a mass to each tracer by integrating the mass density over the corresponding cell. Consequently, the masses of tracers are not equal but reflect the density distribution at the end of the simulation. Further, due to the equal spacing in $\log_{10} r$, the mass resolution ranges from $\Delta m \sim 1.3 \times 10^{-8} M_\odot$ for the innermost tracers to $\Delta m \sim 2.2 \times 10^{-4} M_\odot$ for the outermost ones. The distribution of tracer masses is shown in Figure 1.

Starting from the final position at the end of the simulation, we reconstruct the trajectory of each tracer backward in time based on snapshots of the simulation in intervals of 2 ms until 100 ms after core bounce. A similar approach was used by Wanajo et al. (2018) for 2D simulations. This post-processing is less accurate than tracking the tracers during the simulation on-the-fly, which typically takes much shorter time steps. On the other hand, this procedure takes advantage of the separation between the ejecta and the material ending up in the PNS, so the tracers can be distributed more efficiently. In addition, while numerical errors accumulated during the integration affect the accuracy of a trajectory at early times, the affected part of the trajectory typically corresponds to high temperatures of $T \gtrsim 6.5$ GK for which nuclear statistical equilibrium (NSE) holds. Because nucleosynthesis mostly depends on the evolution after the freeze-out from NSE, it is not much affected by such inaccuracy.

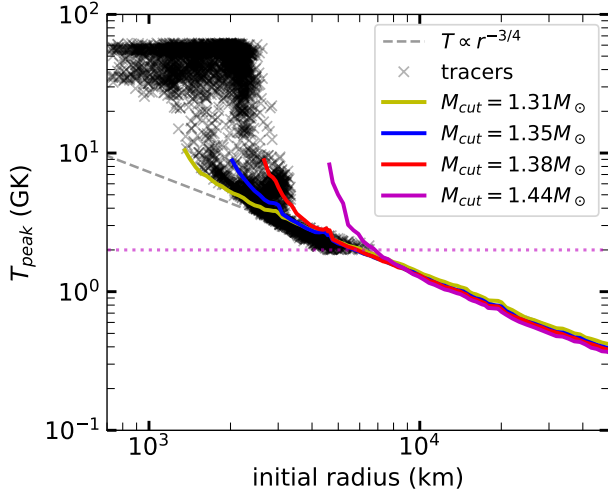


Figure 2. Peak temperature as a function of initial radius. The results for different 1D models are shown as curves. The dotted horizontal line indicates the minimum peak temperature of 2 GK that we require of the selected tracers. See §2.5 for detailed explanation.

Due to ambiguities about the final fate, uncertainties in extrapolation, and numerical integration errors, we cannot use all the extracted tracer histories, but select the tracers based on the following three criteria.

1. We only select tracers that show a positive radial velocity averaged over the last 10 ms of the simulation.¹ Tracers with a negative radial velocity are assumed to become part of the PNS eventually.
2. We only select tracers that reach a temperature above 2 GK. This criterion excludes those tracers that either have not been shocked or have too few post-shock data points for reliable extrapolation. They are found at the outer edge of the simulation domain. We assume that the corresponding material can be reasonably well described by a model in spherical symmetry as indicated in Figure 2 and will be explained in §2.5.
3. We reject those tracers that have a change of entropy exceeding 50% between successive time steps during the last 400 ms of the evolution, which most likely results from integration errors. We still expect this material to be part of the ejecta and redistribute their total mass among the selected tracers, which increases the masses of the latter by a uniform factor of 1.11.

In the end, we have selected 5790 tracers representing $0.1 M_{\odot}$ of the innermost ejecta. We have checked that the

¹ Material with a negative total energy at the end of the simulation still has a chance of being ejected as the energy is raised by pressure forces and turbulent viscous drag of the expanding bubbles. Therefore, we do not use the total energy as a criterion to determine the final fate of a tracer.

distributions of entropy and Y_e for these ejecta are not noticeably affected by the rejection and mass redistribution in our selection of the tracers. We refer readers to Harris et al. (2017) for a detailed discussion of the issues that arise from the initial placement and final selection of tracers.

2.2. Tracer Extrapolation

The simulation was run long enough to determine the PNS properties and important parameters of the explosion. Nucleosynthesis, however, would occur in the expanding material significantly beyond the time $t = t_e$ when the simulation ended. In order to calculate the yields, we need to extrapolate the evolution of radius, temperature, and density of each tracer. We assume that at $t > t_e$, each tracer moves with a fixed velocity $v_r(t_e)$, which is determined from the finite-difference approximation for its dr/dt over the last 5 ms of the simulation. Under this assumption, the radius of a tracer expands linearly as $r(t) = r(t_e) + v_r(t_e)(t - t_e) = r(t_e)[1 + (t - t_e)/\tau]$, where $\tau = r(t_e)/v_r(t_e)$. We further assume that its density and temperature evolve as (e.g., Ning et al. 2007)

$$\rho(t) = \rho(t_e) [1 + (t - t_e)/\tau]^{-2}, \quad (1)$$

and

$$T(t) = T(t_e) [1 + (t - t_e)/\tau]^{-2/3}, \quad (2)$$

respectively. The above extrapolation is far from unique and other authors have used different functional forms. We have also performed calculations with an exponential expansion for $r(t)$ and found no major difference in the nucleosynthesis from the above linear expansion.

2.3. Neutrino Luminosities and Spectra

Neutrinos are critical to the determination of the Y_e of the inner ejecta and play direct roles in the production of the SLR ^{10}Be and other nuclei. Neutrino luminosities and average energies are available from the simulation only for the first ≈ 1.2 s, over which time the energy emitted in neutrinos is 4.2×10^{52} erg. We extrapolate the luminosity for each neutrino species as $L_{\nu_i}(t) = L_{\nu_i}(t_e) \exp[-(t - t_e)/\tau_{\nu_i}]$ beyond the end of the simulation. The decay timescale τ_{ν} is determined by setting the total energy emitted in neutrinos to be the gravitational binding energy of the PNS:

$$\sum_{\nu_i} \int_0^{\infty} L_{\nu_i}(t) dt = (M_{\text{PNS}} - M_G)c^2, \quad (3)$$

where M_{PNS} and M_G are the baryonic and gravitational mass of the PNS, respectively. Following Müller (2015), we take

$$M_G = \frac{\sqrt{1 + (0.336 M_{\text{PNS}}/M_{\odot})} - 1}{0.168} M_{\odot}, \quad (4)$$

which corresponds to a binding energy of 2.25×10^{53} erg for $M_{\text{PNS}} = 1.35 M_{\odot}$. The above procedure gives $\tau_{\nu} = 2$ s.

In addition, we assume that the average neutrino energies $\langle \varepsilon_{\nu_i} \rangle$ linearly decrease at $t > t_e$, reaching zero at 10 s after core bounce. The neutrino spectra are important for the determination of Y_e and for the ν process. For the neutrino reactions on nucleons, the selected reactions listed in Sieverding et al. (2019), and all the reactions affecting the ^{10}Be yield, we follow Keil et al. (2003) and Tamborra et al. (2012) and take the normalized neutrino spectra to be

$$n_{\nu_i}(E) \equiv \left(\frac{\alpha + 1}{\langle \varepsilon_{\nu_i} \rangle} \right)^{\alpha+1} \frac{E^\alpha}{\Gamma(\alpha + 1)} \exp\left(-\frac{(\alpha + 1)E}{\langle \varepsilon_{\nu_i} \rangle}\right), \quad (5)$$

where $\Gamma(\alpha + 1)$ is the Γ function, and α is the so-called “pinching” parameter. We fix α throughout the calculations and use $\alpha = 3.30, 3.12$, and 2.3 for ν_e , $\bar{\nu}_e$, and ν_x ($x = \mu, \tau$; ν_x and $\bar{\nu}_x$ have the same emission properties), respectively. For all the other neutrino-induced reactions, we assume Fermi-Dirac spectra with zero chemical potential and the corresponding average energies $\langle \varepsilon_{\nu_i} \rangle$.

2.4. Corrections of Neutrino Emission

Supernova simulations with state-of-the-art neutrino transport predict that ν_e and $\bar{\nu}_e$ have almost identical luminosities but somewhat different average energies with $\Delta\varepsilon = \langle \varepsilon_{\bar{\nu}_e} \rangle - \langle \varepsilon_{\nu_e} \rangle \approx 2$ MeV during the first second after core bounce (Müller 2019). Because the present 3D simulation used simplified neutrino transport (Müller & Janka 2015), it gives larger values of $\Delta\varepsilon \sim 3\text{--}4$ MeV (see Figure 3). As pointed out in Müller et al. (2019), this caveat leads to inaccurate determination of the Y_e of the inner ejecta by the simulation while the overall dynamics of the explosion is much less affected by the exact differences between the ν_e and $\bar{\nu}_e$ emission. In order to obtain reasonable results of nucleosynthesis, we apply corrections to the neutrino emission properties from the simulation and recalculate the evolution of the Y_e for the selected tracers.

Modifications of the neutrino emission should be consistent with the original hydrodynamic evolution of the tracers. For this purpose, we keep approximately the same neutrino heating rate, which is proportional to (Qian & Woosley 1996)

$$Q = L_{\nu_e} \frac{\langle \varepsilon_{\nu_e}^3 \rangle}{\langle \varepsilon_{\nu_e} \rangle} + L_{\bar{\nu}_e} \frac{\langle \varepsilon_{\bar{\nu}_e}^3 \rangle}{\langle \varepsilon_{\bar{\nu}_e} \rangle}, \quad (6)$$

with $\langle \varepsilon_{\nu_e}^3 \rangle = 1.81 \langle \varepsilon_{\nu_e} \rangle^3$ and $\langle \varepsilon_{\bar{\nu}_e}^3 \rangle = 1.85 \langle \varepsilon_{\bar{\nu}_e} \rangle^3$ being the third moments of the corresponding spectra. To obtain the modified ν_e and $\bar{\nu}_e$ emission properties, which are denoted as the primed quantities below, we specify

$$\langle \varepsilon_{\nu_e} \rangle' = \bar{\varepsilon} - \frac{1}{2} \Delta\varepsilon, \quad \langle \varepsilon_{\bar{\nu}_e} \rangle' = \bar{\varepsilon} + \frac{1}{2} \Delta\varepsilon, \quad (7)$$

where $\Delta\varepsilon = 2$ MeV, $\bar{\varepsilon} = (L_{\nu_e} + L_{\bar{\nu}_e}) / (N_{\nu_e} + N_{\bar{\nu}_e})$, and for example, $N_{\nu_e} = L_{\nu_e} / \langle \varepsilon_{\nu_e} \rangle$. We keep the same pinching parameters α as specified above for the neutrino spectra. Then

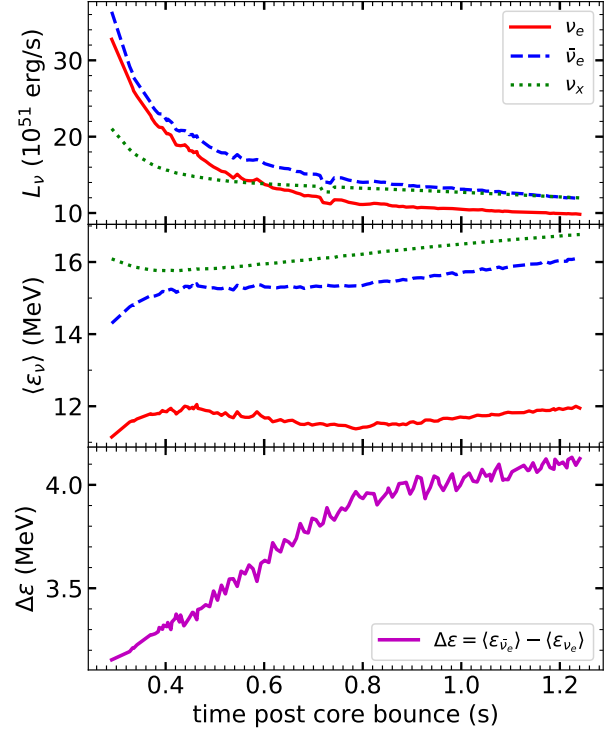


Figure 3. Time evolution of angle-averaged neutrino luminosities and average energies from the 3D simulation of the $11.8 M_\odot$ CCSN. The bottom panel shows the difference in the average energy between ν_e and $\bar{\nu}_e$, which is crucial for determining the Y_e of the inner ejecta and hence the associated nucleosynthesis.

the modified ν_e and $\bar{\nu}_e$ luminosities are obtained from

$$L'_{\nu_e} = L'_{\bar{\nu}_e} = Q \left[\frac{\langle \varepsilon_{\nu_e}^3 \rangle'}{\langle \varepsilon_{\nu_e} \rangle'} + \frac{\langle \varepsilon_{\bar{\nu}_e}^3 \rangle'}{\langle \varepsilon_{\bar{\nu}_e} \rangle'} \right]^{-1}. \quad (8)$$

The above modifications slightly change the luminosities of ν_e and $\bar{\nu}_e$ but enforce the desired difference between their average energies while keeping the neutrino heating rate consistent with the hydrodynamics of the simulation.

As will be discussed in §2.5, we follow the evolution of the Y_e for each tracer by including the pertinent weak reactions, especially ν_e and $\bar{\nu}_e$ absorption on free nucleons, in our nucleosynthesis calculations. We also evaluate the entropy of each tracer using its temperature, density, and composition. Figure 4 compares the distributions of tracer mass in Y_e and entropy for the original (left panel) and modified (right panel) neutrino luminosities and average energies. The values of Y_e are extracted when the temperature drops to 6.5 GK and those of entropy (in units of Boltzmann constant k_B per baryon) are taken when the temperature drops to 2 GK for the last time. The reduced $\Delta\varepsilon$ extends the Y_e range to higher values. This extension is in agreement with other CCSN simulations for similar progenitors, which found mostly proton-rich ejecta (Müller et al. 2012; Wanajo et al. 2018; Vartanyan et al.

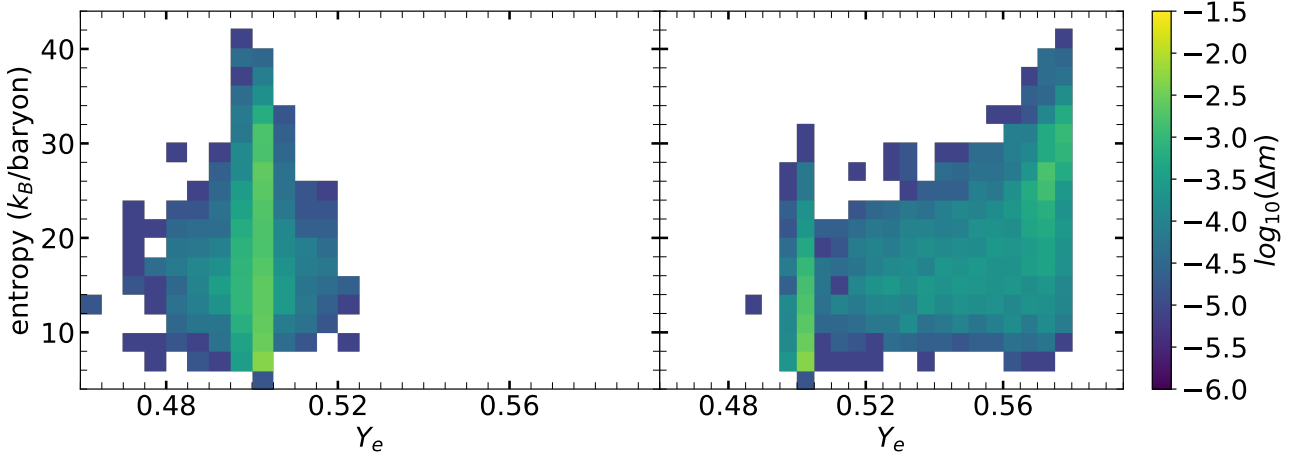


Figure 4. Distributions of tracer mass in Y_e and entropy assuming the original (left panel) and modified (right panel) neutrino emission properties. The prominent presence of matter with $Y_e \approx 0.5$ and low entropy can be traced to its being shocked at large radii.

2019). In contrast, the modified neutrino emission causes little change in the range of entropy, which is mostly determined by the temperature and density. These two quantities are taken to be unaffected by the modifications because we keep the same neutrino heating rate. With the modified neutrino emission, however, higher values of Y_e tend to be associated with higher values of entropy. This trend can be understood because both the Y_e and entropy are mainly set by ν_e and $\bar{\nu}_e$ absorption on free nucleons. Higher entropy corresponds to more occurrences of these reactions, which tend to raise the Y_e more significantly with the reduced $\Delta\epsilon$.

2.5. Nucleosynthesis Calculations

In general, as the CCSN shock propagates further into the outer layers, the dynamical evolution of the shocked ejecta is expected to approach that in an equivalent 1D explosion model. Accordingly, we calculate the nucleosynthesis of the inner ejecta using tracers for as much mass as allowed by the 3D simulation data and treat the outer layers using a 1D model consistent with the 3D simulation. As explained below, this approach is motivated by the comparison of the peak temperature of the shocked ejecta between the 3D simulation and the 1D model.

Figure 2 shows the peak temperature of the tracers as a function of their initial radii at 100 ms after core bounce. There is a large spread in this temperature for tracers with small initial radii.² The spread, however, is reduced drastically for tracers with initial radii of $r_0 > 3000$ km. This result arises because the shock starts to evolve almost spherically once it breaks out of the high-density Fe core. As in-

² Numerical integration errors arise when a tracer remains almost stationary at small radii for an extended period of time. Consequently, the initial position is rather uncertain for those tracers that move near or into the PNS during their evolution.

indicated by the dashed line in Figure 2, for $r_0 > 3000$ km, the peak temperature follows $T_{\text{peak}} \propto r_0^{-3/4}$, which corresponds to a spherical shock dominated by radiation. For comparison, Figure 2 also shows the peak temperature as a function of the initial radius for piston-driven spherical explosion of the same progenitor model with the same explosion energy of 0.3×10^{51} erg but for different values of the mass cut M_{cut} . The results for $M_{\text{cut}} = 1.31\text{--}1.44 M_{\odot}$ converge for $T_{\text{peak}} \lesssim 2$ GK, but the 1D model with $M_{\text{cut}} = 1.35 M_{\odot}$, which matches the PNS mass M_{PNS} found in the 3D simulation, gives the best description of the mean trend for the peak temperature of the tracers up to $T_{\text{peak}} \sim 9$ GK. Based on the above discussion, we use tracers to calculate the nucleosynthesis of the inner ejecta with $T_{\text{peak}} \geq 2$ GK and adopt the 1D model with $M_{\text{cut}} = M_{\text{PNS}} = 1.35 M_{\odot}$ to treat the outer ejecta. As the total mass of the selected tracers, or the inner ejecta, is $M_{\text{in}} = 0.1 M_{\odot}$, the transition between the inner and outer ejecta is at an enclosed mass of $M_{\text{tr}} = M_{\text{PNS}} + M_{\text{in}} = 1.45 M_{\odot}$.

For either the inner or outer ejecta, the associated nucleosynthesis is calculated with the reaction network used in Sieverding et al. (2018), which includes 5300 isotopes. Thermonuclear reaction rates are taken from the ReacLibV2.2 library (Cyburt et al. 2010). When available, β -decay rates are taken from the NUBASE compilation of experimentally determined values (Audi et al. 2017). Otherwise, theoretical β -decay rates from Möller et al. (2003) are used. As in Sieverding et al. (2019), our reaction network includes a large number of neutrino-nucleus reactions, for which the rates are calculated with the appropriate neutrino spectra. When NSE is achieved, the composition is fully determined by the temperature, density, and Y_e . We assume NSE for temperatures above 6.5 GK and use the reaction network to follow the evolution of the composition at lower temperatures.

Regardless of whether NSE is achieved, the evolution of Y_e is always followed with the relevant weak interactions,

including neutrino reactions, e^\pm capture, and β -decay. Rates of e^\pm capture on nuclei are taken from [Langanke & Martínez-Pinedo \(2001\)](#). The most important weak reactions are

$$\nu_e + n \rightleftharpoons e^- + p, \quad \bar{\nu}_e + p \rightleftharpoons e^+ + n. \quad (9)$$

We calculate the rates for the above reactions following [Bruenn \(1985\)](#) and using the axial-vector coupling constant $g_a = 1.2783$ ([Brown et al. 2018](#)). Pauli blocking of e^\pm in the final state is taken into account and detailed balance is enforced for the matrix elements of the forward and reverse reactions. We also include the weak magnetism and nucleon recoil corrections ([Horowitz 2002](#)). The Y_e is very sensitive to the competition between the forward and reverse reactions, and that between the ν_e and $\bar{\nu}_e$ reactions, in Equation (9). Relatively small changes in the relevant rates, such as the weak magnetism and nucleon recoil corrections, can produce significant changes of Y_e to affect nucleosynthesis.

3. NUCLEOSYNTHESIS OF THE INNER EJECTA

We discuss the nucleosynthesis of the inner ejecta in this section. The calculation is based on the tracers for the 3D simulation as described in §2, and covers a total of $0.1 M_\odot$ of the inner ejecta. Due to the limited time, the simulation does not cover matter ejected in the neutrino-driven winds during the long-term cooling of the PNS. We refer readers to the extensive literature for the nucleosynthesis of the neutrino-driven winds (e.g., [Woosley & Hoffman 1992](#); [Qian & Woosley 1996](#); [Hoffman et al. 1997](#); [Roberts et al. 2010](#); [Bliss et al. 2018](#)).

3.1. Conditions of the Inner Ejecta

In general, tracers reaching temperatures of 6.5 GK or above evolve through a phase of NSE and their nucleosynthesis is sensitive to the conditions, especially the Y_e , at the freeze-out from NSE. In contrast, the nucleosynthesis of those tracers never achieving NSE is largely determined by their peak temperatures and is also sensitive to the initial composition.

For tracers evolving through the NSE phase, their freeze-out values of Y_e are mostly set by the competition between the ν_e and $\bar{\nu}_e$ reactions with free nucleons in Equation (9) (e^\pm captures on free nucleons are important only at relatively high densities). As soon as nuclei form, the efficiency of the ν_e and $\bar{\nu}_e$ reactions is suppressed and the Y_e effectively stops changing. Figure 5 shows that with the original neutrino luminosities and spectra from the simulation, there is a relatively narrow distribution for the freeze-out values of Y_e centered around $Y_e \approx 0.5$ with tails extending down to neutron-rich conditions of $Y_e \approx 0.45$ and up to proton-rich conditions of $Y_e \approx 0.52$. Figure 4 also shows that the extreme values of Y_e mostly correspond to low values of $\lesssim 20 k_B/\text{baryon}$ for the entropy. For tracers with $Y_e \approx 0.5$, their values of entropy have a wider range and can reach up to $41 k_B/\text{baryon}$.

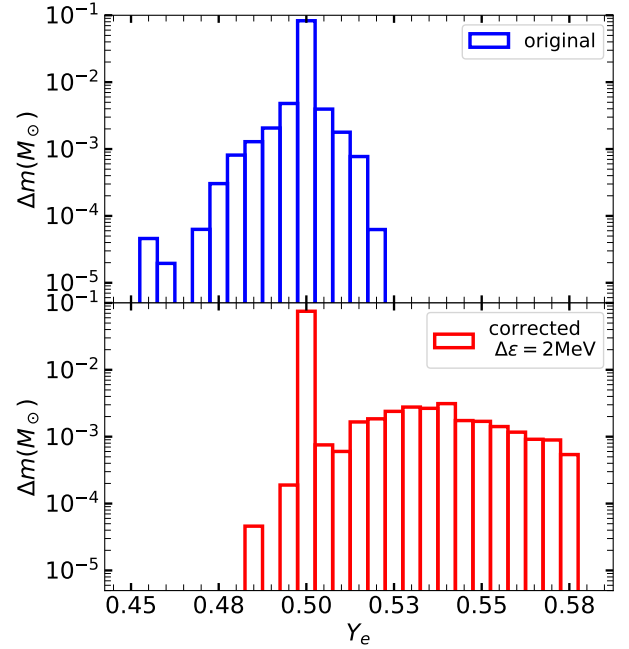


Figure 5. Distributions of tracer mass over the freeze-out values of Y_e assuming the original (top panel) and modified (bottom panel) neutrino emission properties.

With the corrections of neutrino emission described in §2.4, the distribution of Y_e is spread out and shifted to be more proton-rich (see Figure 5). The lowest original value of $Y_e \approx 0.45$ is increased to $Y_e \approx 0.48$. The higher values of Y_e are also correlated with higher values of entropy (see Figure 4). Some of the higher-entropy tracers with the original values of $Y_e \approx 0.5$ now achieve the highest corrected values of $Y_e \approx 0.58$. Based on 2D simulations of similar progenitors, [Wanajo et al. \(2018\)](#) also found the above correlation between Y_e and the asymptotic entropy of the inner ejecta. Our distribution of the corrected Y_e is also in qualitative agreement with their distribution for the $11 M_\odot$ model, which indicates that our corrections of neutrino emission are reasonable. With or without these corrections, most of the inner ejecta still have $Y_e \approx 0.5$. This material is initially at large radii and then ejected by the shock with neither significant dissociation of its nuclei into free nucleons nor substantial exposure to neutrino irradiation. As a result, it essentially retains its initial Y_e .

For tracers with peak temperatures below 6.5 GK, NSE does not apply and the peak temperature is the key parameter for the nucleosynthesis. Figure 2 shows that tracers in the 3D simulation get heated to higher temperatures compared to matter with the same initial radii in the 1D models. The tracer data also show a significant scatter, illustrating that no single 1D model could reproduce the range of conditions found in the 3D simulation. As further illustration of this point, the

1D models do not include material that falls close to the PNS, reaches temperatures in excess of 10 GK, and is still ejected eventually. For comparison with the 3D simulation only, we also calculate the nucleosynthesis of the inner ejecta using the adopted 1D model. In addition to the above difference in the peak temperature, matter ejected from near the PNS in the 3D simulation has more extreme values of Y_e than that in our adopted 1D model. Both these differences are among the key factors differentiating the nucleosynthesis results for the two types of models.

3.2. Results for the Inner Ejecta

Figure 6 shows the final production factors X_*/X_{\odot} for the stable isotopes after all decay is completed, where X_* is the mass fraction of a stable isotope produced relative to the total mass ($M_{\text{in}} = 0.1 M_{\odot}$) of the inner ejecta and X_{\odot} is the corresponding solar mass fraction given by [Asplund et al. \(2009\)](#). The shaded bands include isotopes with production factors above 0.1 times the highest value. For these isotopes, $\geq 10\%$ of their solar inventory could be contributed by the CCSNe of concern. It is instructive to compare the results calculated with the original (top panel) and corrected (bottom panel) neutrino emission properties. The more neutron-rich conditions in the former case (see Figure 4) lead to the high production factors for the p -nuclei ^{74}Se , ^{78}Kr , and ^{92}Mo , which is in agreement with the parametric studies of [Hoffman et al. \(1996\)](#) and the calculations of [Wanajo et al. \(2018\)](#) based on 2D simulations for similar conditions. Here these isotopes are produced in quasi-statistical equilibrium clusters for $Y_e \approx 0.485$ and low values of entropy (~ 10 – $20 k_B/\text{baryon}$). The neutron-rich conditions are also responsible for the high production factors for ^{62}Ni , ^{64}Zn , and ^{90}Zr (see also [Hoffman et al. 1996](#)).³ As discussed above, however, we consider that the results calculated with the corrected neutrino emission properties are more realistic. In this case, more tracers freeze out from NSE with $Y_e \geq 0.5$ and higher values of entropy. Consequently, there is no significant production for any of the p -nuclei mentioned above. Instead, the largest production factors are obtained for ^{45}Sc , ^{60}Ni , and ^{64}Zn . In addition, mostly because there are more ^4He nuclei left at the end, the maximum production factor is smaller than that in the case with the original neutrino emission properties. The yields from the tracers with the corrected neutrino emission properties are summarized in Table 1, which only includes stable isotopes up to mass number $A = 100$ and with yields exceeding $10^{-10} M_{\odot}$. The complete

yields are provided as supplemental material in machine-readable format.

The high production factor for ^{45}Sc in proton-rich ejecta resembles the previous results of, e.g., [Pruet et al. \(2005\)](#) and [Fröhlich et al. \(2006\)](#). Starting mostly from ^{40}Ca , which is abundant at the freeze-out from NSE, a sequence of proton captures produces highly neutron-deficient nuclei up to ^{45}Cr . Due to the very low proton-separation energy of ^{46}Mn , the reaction flow needs to wait for the β -decay of ^{45}Cr with a half-life of 64 ms. Because matter cools down considerably on this timescale, charged-particle reactions quickly freeze out and the decay chain of ^{45}Cr eventually produces ^{45}Sc . In addition, sufficiently fast expansion is required to prevent proton captures on ^{45}V along the decay chain so that a large production factor of ^{45}Sc can be obtained. Such expansion is found for the higher-entropy ejecta in multi-D simulations. Unfortunately, the longest half-life along the decay chain to ^{45}Sc is only ≈ 3 h for ^{45}Ti , which is too short to allow late-time observations.

The production of ^{64}Zn depends strongly on Y_e . For tracers freezing out from NSE with $Y_e \approx 0.47$ – 0.48 , ^{64}Zn is produced almost directly from NSE. For proton-rich conditions, ^{64}Zn is made as ^{64}Ga and ^{64}Ge by a sequence of proton capture reactions following the particle-rich freeze-out. Relatively large production factors for ^{64}Zn were also found by [Wanajo et al. \(2018\)](#). Because the production of ^{64}Zn is dominated by tracers achieving NSE, it is insensitive to the initial composition of the progenitor. Consequently, the large production factor of ^{64}Zn for our progenitor model with an initial solar metallicity may also help explain the observations of $[\text{Zn}/\text{Fe}] = \log(\text{Zn}/\text{Fe}) - \log(\text{Zn}/\text{Fe})_{\odot}$ in metal-poor stars. [Ezzeddine et al. \(2019\)](#) recently measured $[\text{Zn}/\text{Fe}] = 0.8 \pm 0.25$ for an ultra-metal-poor star and had difficulty reconciling this result with the predictions of 1D CCSN models. Based on the 3D simulation, we find that our model can provide $[\text{Zn}/\text{Fe}] = 1.11$ and 0.43 with the original and corrected neutrino emission properties, respectively. In contrast, our adopted 1D model gives a much lower value of $[\text{Zn}/\text{Fe}] = 0.10$. Our results indicate that multi-D dynamics and accurate neutrino emission properties are crucial to understanding the particular measurement of [Ezzeddine et al. \(2019\)](#) and the general observations of $[\text{Zn}/\text{Fe}]$ in metal-poor stars. The production of Zn and Fe by metal-free and metal-poor CCSNe certainly merits detailed investigation with 3D simulations and accurate neutrino transport.

The inner ejecta also produce ^{56}Ni and ^{44}Ti , which are important due to the observational signatures from their radioactivity. Our tracer calculations give $0.016 M_{\odot}$ and $0.018 M_{\odot}$ of ^{56}Ni with the original and corrected neutrino emission properties, respectively. By comparison, our adopted 1D model gives $\approx 0.023 M_{\odot}$, which is insensitive

³ The isotope ^{62}Ni can be directly produced from NSE for $Y_e \approx 0.45$, which is close to its charge-to-mass ratio $Z/A = 0.452$. Most of its final yield, however, is produced as ^{62}Zn with a half-life of ≈ 9 h. With a higher value of $Z/A = 0.484$, ^{62}Zn is produced in a larger fraction of the material undergoing complete Si-burning and achieving NSE. The above two modes of ^{62}Ni production were also noted by [Hoffman et al. \(1996\)](#).

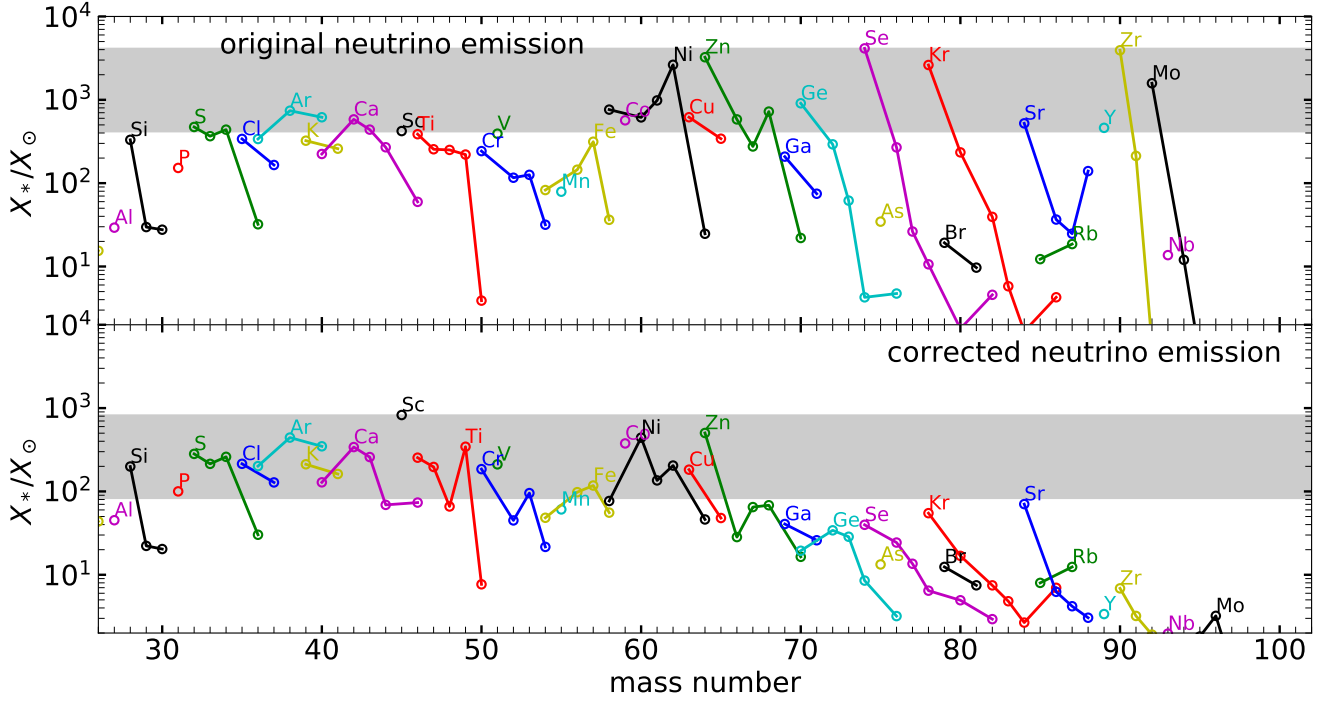


Figure 6. Production factors for stable isotopes made in the inner ejecta with the original (top panel) and corrected (bottom panel) neutrino emission properties. The mass fraction X_* is relative to the total mass of $0.1 M_\odot$ for the inner ejecta. The shaded bands include isotopes with production factors above 0.1 times the highest value. Isotopes of the same element are connected by line segments and colored for better visibility.

to the neutrino emission properties. All of the above values⁴ are in approximate agreement with what is expected from similar low-mass CCSNe (Müller et al. 2016; Sukhbold et al. 2016; Ebinger et al. 2019) and with the observed lower ^{56}Ni production by less energetic events (Hamuy 2003; Pejcha & Prieto 2015; Müller et al. 2017). The larger ^{56}Ni yield in the 1D model can be understood as follows. Although the amount of matter reaching temperatures above 6.5 GK is $0.028 M_\odot$ for the 3D simulation and only $0.014 M_\odot$ for the 1D model, the amount of ^{56}Ni produced from this NSE component undergoing complete Si burning is almost the same for both models. This result can be traced to the more extreme values of Y_e and the much larger mass fraction of α particles at the freeze-out of the 3D tracers, both of which reduce the production of ^{56}Ni . In addition, the amount of matter reaching temperatures of $\sim 3\text{--}6.5$ GK in the 3D simulation is smaller than that in the 1D model. The extra production of ^{56}Ni for the latter mostly originates in this component undergoing incomplete Si-burning.

The production of ^{44}Ti is generally sensitive to a combination of factors. The tracer calculations with the original neu-

trino emission properties give $3.73 \times 10^{-5} M_\odot$ of ^{44}Ti , to be compared with $1.13 \times 10^{-5} M_\odot$ for the 1D model. This result can be explained by the higher values of entropy and the more particle-rich freeze-out for the tracers, both of which help the ^{44}Ti production. With the corrected neutrino emission properties, however, the higher-entropy tracers are more proton-rich, which increases the production of ^{45}Sc and ^{64}Zn at the expense of ^{44}Ti . As a result, the ^{44}Ti yield of $1.58 \times 10^{-5} M_\odot$ is only slightly above that for the 1D model, which is again insensitive to the neutrino emission properties. Therefore, while the higher values of entropy found in 3D simulations generally tend to increase the ^{44}Ti yield, the more extreme values of Y_e found in such models can also have a large impact. The resulting uncertainty in the ^{44}Ti yield can be removed only by 3D simulations with accurate neutrino transport. Such simulations are also required to address whether the 3D explosion of an appropriate progenitor can account for the rather high ^{44}Ti yield of $\sim (0.3\text{--}3.9) \times 10^{-4} M_\odot$ inferred for SN 1987A (Boggs et al. 2015; Seitenzahl et al. 2014; Grebnev et al. 2012).

4. NUCLEOSYNTHESIS OF THE OUTER EJECTA AND TOTAL CCSN YIELDS

As discussed in §2.5, we use our adopted 1D model to calculate the nucleosynthesis of the outer ejecta, which are separated from the inner ejecta at an enclosed mass of $M_{\text{tr}} =$

⁴ The mass resolution is typically $4 \times 10^{-3} M_\odot$ for the 1D model, which is much coarser than that of the tracers. This difference results in different sampling of nucleosynthesis conditions, which may also slightly affect the yields.

Table 1. Yields^a of stable isotopes in M_{\odot} from the tracers with the corrected neutrino emission properties

¹ H	1.55×10^{-3}	²⁹ Si	1.01×10^{-4}	⁴⁷ Ti	7.28×10^{-6}	⁶⁵ Cu	1.39×10^{-6}	⁸¹ Br	6.05×10^{-9}
⁴ He	9.47×10^{-3}	³⁰ Si	6.38×10^{-5}	⁴⁸ Ti	2.47×10^{-5}	⁶⁴ Zn	8.70×10^{-5}	⁷⁸ Kr	3.59×10^{-9}
⁷ Li	5.68×10^{-10}	³¹ P	9.97×10^{-5}	⁴⁹ Ti	9.62×10^{-6}	⁶⁶ Zn	2.26×10^{-6}	⁸⁰ Kr	7.16×10^{-9}
¹¹ B	8.88×10^{-10}	³² S	1.57×10^{-2}	⁵⁰ Ti	5.69×10^{-8}	⁶⁷ Zn	7.94×10^{-7}	⁸² Kr	3.19×10^{-9}
¹² C	8.12×10^{-5}	³³ S	9.84×10^{-5}	⁵¹ V	1.28×10^{-5}	⁶⁸ Zn	4.25×10^{-6}	⁸³ Kr	3.04×10^{-9}
¹³ C	2.28×10^{-8}	³⁴ S	6.93×10^{-4}	⁵⁰ Cr	2.29×10^{-5}	⁷⁰ Zn	3.03×10^{-8}	⁸⁴ Kr	5.23×10^{-9}
¹⁴ N	3.62×10^{-7}	³⁶ S	2.09×10^{-7}	⁵² Cr	1.11×10^{-4}	⁶⁹ Ga	1.68×10^{-7}	⁸⁶ Kr	7.74×10^{-9}
¹⁵ N	1.16×10^{-6}	³⁵ Cl	1.25×10^{-4}	⁵³ Cr	2.73×10^{-5}	⁷¹ Ga	6.02×10^{-8}	⁸⁵ Rb	4.42×10^{-9}
¹⁶ O	1.87×10^{-2}	³⁷ Cl	2.36×10^{-5}	⁵⁴ Cr	1.05×10^{-6}	⁷⁰ Ge	5.10×10^{-8}	⁸⁷ Rb	2.88×10^{-9}
¹⁷ O	2.73×10^{-7}	³⁶ Ar	2.00×10^{-3}	⁵⁵ Mn	1.31×10^{-4}	⁷² Ge	2.54×10^{-7}	⁸⁴ Sr	3.22×10^{-9}
¹⁸ O	2.36×10^{-8}	³⁸ Ar	8.41×10^{-4}	⁵⁴ Fe	5.60×10^{-4}	⁷³ Ge	4.11×10^{-8}	⁸⁶ Sr	2.46×10^{-9}
¹⁹ F	1.04×10^{-7}	⁴⁰ Ar	9.63×10^{-7}	⁵⁶ Fe	1.85×10^{-2}	⁷⁴ Ge	3.19×10^{-8}	⁸⁷ Sr	7.39×10^{-10}
²⁰ Ne	3.64×10^{-3}	³⁹ K	1.20×10^{-4}	⁵⁷ Fe	5.14×10^{-4}	⁷⁶ Ge	8.03×10^{-9}	⁸⁸ Sr	5.43×10^{-9}
²¹ Ne	3.80×10^{-6}	⁴¹ K	6.88×10^{-6}	⁵⁸ Fe	7.17×10^{-6}	⁷⁵ As	1.44×10^{-8}	⁸⁹ Y	1.70×10^{-9}
²² Ne	1.30×10^{-6}	⁴⁰ Ca	1.26×10^{-3}	⁵⁹ Co	2.04×10^{-4}	⁷⁴ Se	7.42×10^{-9}	⁹⁰ Zr	1.20×10^{-8}
²³ Na	4.70×10^{-5}	⁴² Ca	2.33×10^{-5}	⁵⁸ Ni	6.27×10^{-4}	⁷⁶ Se	2.93×10^{-8}	⁹¹ Zr	6.23×10^{-10}
²⁴ Mg	8.90×10^{-4}	⁴³ Ca	3.75×10^{-6}	⁶⁰ Ni	1.43×10^{-3}	⁷⁷ Se	1.01×10^{-8}	⁹² Zr	3.01×10^{-10}
²⁵ Mg	1.18×10^{-4}	⁴⁴ Ca	1.59×10^{-5}	⁶¹ Ni	1.48×10^{-5}	⁷⁸ Se	5.59×10^{-9}	⁹⁴ Zr	3.10×10^{-10}
²⁶ Mg	1.16×10^{-4}	⁴⁶ Ca	1.50×10^{-8}	⁶² Ni	9.02×10^{-5}	⁸⁰ Se	1.17×10^{-8}	⁹³ Nb	1.87×10^{-10}
²⁷ Al	1.66×10^{-4}	⁴⁵ Sc	5.39×10^{-6}	⁶⁴ Ni	1.48×10^{-6}	⁸² Se	5.52×10^{-9}	⁹² Mo	1.55×10^{-10}
²⁸ Si	2.14×10^{-2}	⁴⁶ Ti	1.02×10^{-5}	⁶³ Cu	1.33×10^{-5}	⁷⁹ Br	6.79×10^{-9}	⁹⁶ Mo	1.34×10^{-10}

^a Yields less than $10^{-10} M_{\odot}$ or for $A > 100$ are not shown. A complete table is available as supplemental material.

$1.45 M_{\odot}$. The separation is located in the O/Ne shell and has a peak temperature of $T_{\text{peak}} = 2.2$ GK in the 1D model, which fits well with our lower limit of $T_{\text{peak}} = 2$ GK for the selected tracers representing the inner ejecta.⁵

The ν process, i.e., the production of isotopes in the outer ejecta due to neutrino-nucleus reactions, leads to important nucleosynthetic signatures, including the production of the SLR ^{10}Be . This process depends on both the neutrino emission from the PNS and the shock propagation through the outer ejecta, thereby providing a direct link between the inner evolution described by the 3D simulation and the outer evolution described by our adopted 1D model. We use the corrected neutrino emission properties to calculate the rates of neutrino-nucleus reactions for the ν process. Sieverding et al. (2019) found that the early phase of neutrino emission is important for this process. This phase is automatically included in our calculations.

4.1. Total CCSN Yields

Combining the results for the inner and outer ejecta with the corrected neutrino emission properties, we give the total yields of the CCSN in Table 2, which only includes stable isotopes up to $A = 100$ and with yields exceeding $10^{-10} M_{\odot}$.

⁵ A small amount of material with $T_{\text{peak}} = 2.0$ – 2.2 GK is represented by both tracers and the 1D model. This overlap is consistent with the scatter of tracers at $T_{\text{peak}} \sim 2$ GK in Figure 2.

The complete table is provided as supplemental material in machine-readable format. The contributions from the outer ejecta can be obtained from comparing Tables 1 and 2.

The top panel of Figure 7 shows the production factors of the stable isotopes in the entire CCSN ejecta, where the mass fraction of each isotope is relative to the total ejecta mass of $9.04 M_{\odot}$.⁶ The largest production factor of 16.5 corresponds to ^{45}Sc . Isotopes with production factors exceeding half of this value are ^{11}B , $^{38,40}\text{Ar}$, ^{59}Co , ^{60}Ni , and ^{64}Zn . The shaded band indicates production factors above 0.1 times the highest value and includes the majority of the stable isotopes between B and Ge. These results suggest that had $11.8 M_{\odot}$ CC-SNe made all of the ^{45}Sc in the solar inventory, they would have also contributed $\gtrsim 10\%$ of the majority of the other stable isotopes between B and Ge. In particular, with a production factor of 3.01 for ^{16}O , they would have contributed $\approx 18\%$ of this important isotope. The top panel of Figure 7 also shows that except for ^{96}Mo , the stable isotopes with $A \sim 90$ – 100 have production factors close to unity. These isotopes simply reflect the initial composition of the ejecta. This result also extends to nearly all of those stable isotopes with $A > 100$ (not shown) because the corresponding initial composition is essentially unaffected by the pre-CCSN

⁶ Note that a total of $1.41 M_{\odot}$ of the H envelope are lost through winds during the pre-CCSN evolution.

Table 2. Total CCSN yields^a of stable isotopes in M_{\odot} with the corrected neutrino emission properties

¹ H	5.31	²⁸ Si	2.75×10^{-2}	⁴⁹ Ti	1.13×10^{-5}	⁷⁰ Zn	1.93×10^{-7}	⁸⁷ Rb	5.90×10^{-8}
² H	1.23×10^{-10}	²⁹ Si	4.78×10^{-4}	⁵⁰ Ti	1.91×10^{-6}	⁶⁹ Ga	7.89×10^{-7}	⁸⁴ Sr	5.60×10^{-9}
³ He	3.22×10^{-4}	³⁰ Si	3.13×10^{-4}	⁵¹ V	1.60×10^{-5}	⁷¹ Ga	4.82×10^{-7}	⁸⁶ Sr	5.71×10^{-8}
⁴ He	3.33	³¹ P	1.79×10^{-4}	⁵⁰ Cr	2.93×10^{-5}	⁷⁰ Ge	7.14×10^{-7}	⁸⁷ Sr	3.71×10^{-8}
⁷ Li	1.31×10^{-7}	³² S	1.86×10^{-2}	⁵² Cr	2.41×10^{-4}	⁷² Ge	1.03×10^{-6}	⁸⁸ Sr	4.25×10^{-7}
⁹ Be	1.42×10^{-10}	³³ S	1.24×10^{-4}	⁵³ Cr	4.25×10^{-5}	⁷³ Ge	2.95×10^{-7}	⁸⁹ Y	1.02×10^{-7}
¹⁰ B	1.56×10^{-9}	³⁴ S	8.38×10^{-4}	⁵⁴ Cr	6.29×10^{-6}	⁷⁴ Ge	9.94×10^{-7}	⁹⁰ Zr	1.24×10^{-7}
¹¹ B	3.23×10^{-7}	³⁶ S	1.43×10^{-6}	⁵⁵ Mn	2.47×10^{-4}	⁷⁶ Ge	1.63×10^{-7}	⁹¹ Zr	2.65×10^{-8}
¹² C	5.77×10^{-2}	³⁵ Cl	1.56×10^{-4}	⁵⁴ Fe	1.16×10^{-3}	⁷⁵ As	1.51×10^{-7}	⁹² Zr	3.96×10^{-8}
¹³ C	6.98×10^{-4}	³⁷ Cl	3.95×10^{-5}	⁵⁶ Fe	2.84×10^{-2}	⁷⁴ Se	1.70×10^{-8}	⁹⁴ Zr	4.02×10^{-8}
¹⁴ N	2.68×10^{-2}	³⁶ Ar	2.52×10^{-3}	⁵⁷ Fe	7.78×10^{-4}	⁷⁶ Se	2.03×10^{-7}	⁹³ Nb	1.74×10^{-8}
¹⁵ N	2.03×10^{-5}	³⁸ Ar	9.47×10^{-4}	⁵⁸ Fe	1.06×10^{-4}	⁷⁷ Se	1.32×10^{-7}	⁹² Mo	8.02×10^{-9}
¹⁶ O	1.66×10^{-1}	⁴⁰ Ar	1.71×10^{-6}	⁵⁹ Co	2.61×10^{-4}	⁷⁸ Se	3.73×10^{-7}	⁹⁴ Mo	5.41×10^{-9}
¹⁷ O	5.34×10^{-5}	³⁹ K	1.51×10^{-4}	⁵⁸ Ni	1.05×10^{-3}	⁸⁰ Se	7.46×10^{-7}	⁹⁵ Mo	9.47×10^{-9}
¹⁸ O	7.44×10^{-4}	⁴¹ K	9.81×10^{-6}	⁶⁰ Ni	1.62×10^{-3}	⁸² Se	1.16×10^{-7}	⁹⁶ Mo	1.71×10^{-8}
¹⁹ F	7.21×10^{-6}	⁴⁰ Ca	1.78×10^{-3}	⁶¹ Ni	3.35×10^{-5}	⁷⁹ Br	1.43×10^{-7}	⁹⁷ Mo	5.68×10^{-9}
²⁰ Ne	4.54×10^{-2}	⁴² Ca	2.73×10^{-5}	⁶² Ni	1.29×10^{-4}	⁸¹ Br	1.25×10^{-7}	⁹⁸ Mo	1.47×10^{-8}
²¹ Ne	1.28×10^{-4}	⁴³ Ca	4.67×10^{-6}	⁶⁴ Ni	2.22×10^{-5}	⁷⁸ Kr	6.93×10^{-9}	¹⁰⁰ Mo	5.81×10^{-9}
²² Ne	3.16×10^{-3}	⁴⁴ Ca	2.86×10^{-5}	⁶³ Cu	3.21×10^{-5}	⁸⁰ Kr	3.16×10^{-8}	⁹⁶ Ru	2.08×10^{-9}
²³ Na	1.59×10^{-3}	⁴⁶ Ca	8.20×10^{-8}	⁶⁵ Cu	6.51×10^{-6}	⁸² Kr	1.67×10^{-7}	⁹⁸ Ru	7.23×10^{-10}
²⁴ Mg	9.54×10^{-3}	⁴⁵ Sc	5.86×10^{-6}	⁶⁴ Zn	9.63×10^{-5}	⁸³ Kr	1.39×10^{-7}	⁹⁹ Ru	4.97×10^{-9}
²⁵ Mg	1.81×10^{-3}	⁴⁶ Ti	1.24×10^{-5}	⁶⁶ Zn	9.69×10^{-6}	⁸⁴ Kr	6.63×10^{-7}	¹⁰⁰ Ru	5.25×10^{-9}
²⁶ Mg	1.89×10^{-3}	⁴⁷ Ti	9.26×10^{-6}	⁶⁷ Zn	2.19×10^{-6}	⁸⁶ Kr	2.47×10^{-7}		
²⁷ Al	1.15×10^{-3}	⁴⁸ Ti	4.56×10^{-5}	⁶⁸ Zn	9.93×10^{-6}	⁸⁵ Rb	1.33×10^{-7}		

^aYields less than $10^{-10} M_{\odot}$ or for $A > 100$ are not shown. A complete table is available as supplemental material.

evolution of the progenitor or the CCSN process. The small number of exceptions are the isotopes produced by the γ process (e.g., ¹⁵²Gd) and the ν process (e.g., ¹³⁸La and ¹⁸⁰Ta) during the shock propagation.

The isotope with the largest production factor, ⁴⁵Sc, is produced in the inner ejecta. Other major isotopes produced by the inner ejecta can be identified by comparing the shaded band in Figure 7 with that in the bottom panel of Figure 6 (note that the mass fraction in the latter figure is relative to the total inner ejecta mass of $0.1 M_{\odot}$, but this normalization does not affect the placement of the shaded band). To see the effects of the 3D explosion, we show in the bottom panel of Figure 7 the ratios of yields from our combined model to those from the adopted 1D model. Isotopes that are mostly contributed by the outer ejecta are unaffected by the difference in the explosion. These isotopes include the elements up to Si. The largest change due to the 3D explosion is the increase of the ⁴⁵Sc yield by an order of magnitude. The yields of ⁴³Ca and ^{47,49}Ti increase by factors of 3–4. With a large amount of matter freezing out from the proton-rich NSE in the 3D simulation, the yield pattern of the Ni isotopes changes and the ⁶⁰Ni yield increases by more than a factor of 3. The yield of ⁵⁹Co increases by a factor of 2.3 under the same conditions. In addition, the 3D proton-rich component

of the inner ejecta produces ~ 2 –3 times more of ⁶⁴Zn and the light p -isotopes ⁷⁴Se and ⁷⁸Kr. The above results can be largely traced to the more proton-rich conditions of the inner ejecta due to more neutrino processing in 3D.

4.2. Uncertainties of ¹⁰Be Production

In addition to the stable isotopes, our combined model gives the yields of SLRs, which will be used in §5 to explore the $11.8 M_{\odot}$ CCSN as a candidate trigger for the formation of the solar system (Banerjee et al. 2016). In this subsection, we discuss the production of the SLR ¹⁰Be and the associated uncertainties. As suggested by Banerjee et al. (2016), CCSNe might be a significant source of ¹⁰Be in the interstellar medium (ISM), which contradicts the common assumption that this SLR can only be produced by high-energy collisions between nuclei. Therefore, our discussion has other implications even if the $11.8 M_{\odot}$ CCSN might not have been the trigger for solar system formation.

The CCSN production of ¹⁰Be proceeds predominantly through the neutral-current (NC) reaction ¹²C($\nu, \nu'pp$)¹⁰Be and the charged-current (CC) reactions ¹²C($\bar{\nu}_e, e^+np$)¹⁰Be and ¹¹C($\bar{\nu}_e, e^+p$)¹⁰Be. The role of ¹²C($\bar{\nu}_e, e^+np$)¹⁰Be was noted by Takigawa et al. (2008). All of these reactions occur in the relatively thin C/O shell of the $11.8 M_{\odot}$ CCSN,

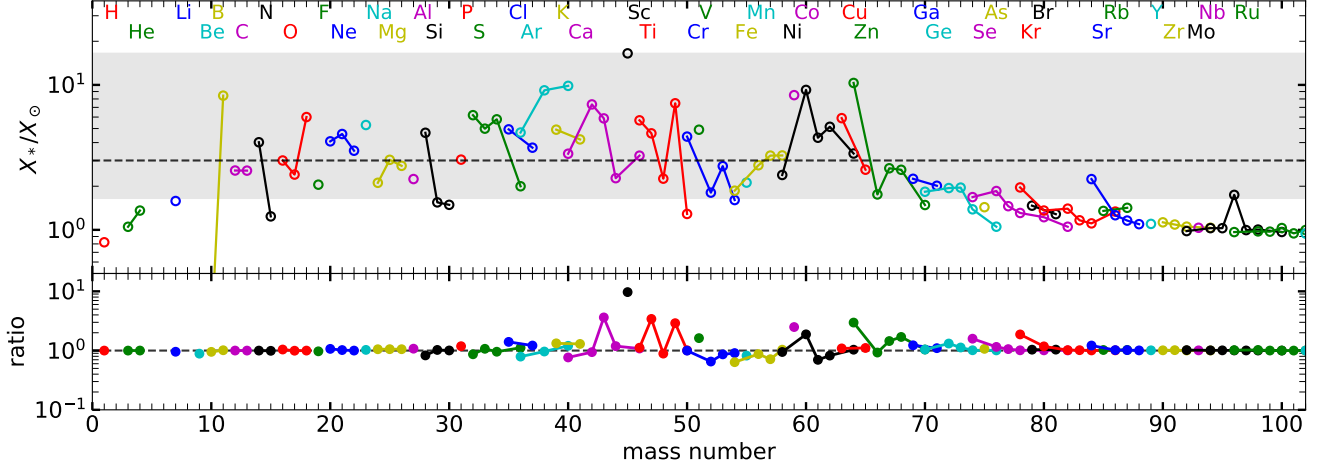


Figure 7. Production factors for stable isotopes in the entire CCSN ejecta with the corrected neutrino emission properties (top panel) and ratios of yields from our combined model to those from the adopted 1D model (bottom panel). The mass fraction X_* is relative to the total ejecta mass of $9.04 M_{\odot}$. The shaded band includes isotopes with production factors above 0.1 times the highest value. The dashed line indicates the production factor of ^{16}O . Isotopes of the same element are connected by line segments and colored for better visibility.

where the peak post-shock temperature is just below 1 GK. This material is part of the outer ejecta and is not affected by the details of the explosion so long as an appropriate explosion energy is used. We adopt the cross sections of Yoshida et al. (2008) based on shell-model calculations for $^{12}\text{C}(\nu, \nu' pp)^{10}\text{Be}$ and $^{12}\text{C}(\bar{\nu}_e, e^+ np)^{10}\text{Be}$, and the cross section of Sieverding et al. (2018) based on random phase approximation for $^{11}\text{C}(\bar{\nu}_e, e^+ p)^{10}\text{Be}$. The $\bar{\nu}_e$ -induced CC reactions typically have larger cross sections than the NC reaction induced by all neutrino species. As a result, the NC and CC channels make approximately the same contributions to the production of ^{10}Be . In contrast, the ν_e -induced CC reaction $^{10}\text{Be}(\nu_e, e^-)^{10}\text{B}$ destroys ^{10}Be . The cross section of this reaction is taken from Sieverding et al. (2018). The destruction of ^{10}Be by $^{10}\text{Be}(p, \alpha)^7\text{Li}$ can also be important. By default, we use the rate in the JINA REALCLIB library (Cyburt et al. 2010) for this reaction, which is based on the estimates of Wagoner (1969) from the statistical model.

The nominal yield of ^{10}Be from the $11.8 M_{\odot}$ CCSN is $6.08 \times 10^{-11} M_{\odot}$ (see the first entry in Table 3). There are, however, large uncertainties in this yield. One factor is the large uncertainty in the rate of $^{10}\text{Be}(p, \alpha)^7\text{Li}$ (Iliadis et al. 2010). For example, we have repeated the calculations leaving out this reaction but with no other changes and found a factor of ≈ 3 increase in the ^{10}Be yield (see Table 3). Further uncertainties in this yield come from the possibility of neutrino flavor oscillations that could significantly alter the effective neutrino energy spectra for the production and destruction of ^{10}Be . Whereas flavor oscillations do not affect the NC production, the CC production (destruction) could be significantly enhanced if $\bar{\nu}_x$ (ν_x) with harder spectra (see Figure 3) were converted into $\bar{\nu}_e$ (ν_e). Similar effects were dis-

Table 3. Uncertainties in the ^{10}Be yield

$^{10}\text{Be}(p, \alpha)^7\text{Li}$	Flavor Oscillations	^{10}Be Yield ($10^{-10} M_{\odot}$)
default	no	0.608
off	no	1.80
default	$\bar{\nu}_e \leftrightarrow \bar{\nu}_x$	1.99
off	$\bar{\nu}_e \leftrightarrow \bar{\nu}_x$	5.06
default	$\nu_e \leftrightarrow \nu_x$	0.348
off	$\nu_e \leftrightarrow \nu_x$	1.48

cussed previously for the ν process in general (e.g., Yoshida et al. 2006; Wu et al. 2015). For illustration, we consider two extreme scenarios where either $\bar{\nu}_e \leftrightarrow \bar{\nu}_x$ or $\nu_e \leftrightarrow \nu_x$ oscillations cause the corresponding neutrino species to exchange their spectra, thereby having the largest effect on the ^{10}Be production or destruction. As shown in Table 3, when $^{10}\text{Be}(p, \alpha)^7\text{Li}$ is (not) included in the calculations, $\bar{\nu}_e \leftrightarrow \bar{\nu}_x$ oscillations can increase the ^{10}Be yield by a factor of ≈ 3.3 (2.8), whereas $\nu_e \leftrightarrow \nu_x$ oscillations can decrease it by a factor of ≈ 1.7 (1.2).

Without neutrino flavor oscillations, our nominal ^{10}Be yield from the $11.8 M_{\odot}$ CCSN is ~ 5 times smaller than the value of $3.26 \times 10^{-10} M_{\odot}$ obtained by Banerjee et al. (2016). Compared to our calculations, that work used a smaller explosion energy of 0.1×10^{50} erg and somewhat different neutrino spectra. The main differences, however, are that it ignored $^{10}\text{Be}(p, \alpha)^7\text{Li}$, $^{10}\text{Be}(\nu_e, e^-)^{10}\text{B}$, and the $\bar{\nu}_e$ -induced CC production of ^{10}Be . The destruction of ^{10}Be by the first two reactions overwhelms the additional production by $\bar{\nu}_e$, which explains our much smaller nominal yield.

Banerjee et al. (2016) also calculated ^{10}Be yields for more massive CCSNe. Those yields should be checked by detailed

calculations including those reactions ignored by that work. The effects of neutrino spectra and flavor oscillations should be explored as well. Such efforts are required to quantify CCSNe as a source of ^{10}Be in the ISM.

5. OVERALL PRODUCTION OF SLRS

In this section we discuss the yields of SLRs from the $11.8 M_{\odot}$ CCSN based on our combined model and the implications for the abundances of these SLRs in the ESS. We give these yields in Table 4 along with those obtained by Banerjee et al. (2016) using a 1D model. It can be seen that our yields and theirs are close for ^{60}Fe , ^{107}Pd , ^{135}Cs , ^{182}Hf , and ^{205}Pb , but differ greatly for ^{10}Be , ^{26}Al , ^{36}Cl , ^{41}Ca , and ^{53}Mn . The difference for ^{10}Be is discussed in detail in §4.2. The similarities and differences for the other SLRs can be traced to their regions of production. Figure 8 shows the cumulative fraction of the yield for each SLR as a function of the enclosed mass for our combined model. Because the transition between the inner and outer ejecta is at the enclosed mass of $M_{\text{tr}} = 1.45 M_{\odot}$, almost all of the ^{36}Cl , ^{41}Ca , and ^{53}Mn are attributed to the inner ejecta modeled by our 3D simulation. In contrast, nearly all of the ^{60}Fe , ^{107}Pd , ^{135}Cs , ^{182}Hf , and ^{205}Pb are attributed to the outer ejecta covered by our adopted 1D model. Whereas the details of the explosion, especially the mass cut, have a large impact on the production of the SLRs dominantly attributed to the inner ejecta, the yields of those SLRs dominantly attributed to the outer ejecta largely reflect the weak s -process nucleosynthesis during the pre-CCSN evolution and are not significantly affected by the explosion. The mass cut determined from our 3D simulation is at the enclosed mass of $M_{\text{cut}} = 1.35 M_{\odot}$. Banerjee et al. (2016), however, chose a significantly larger mass cut at $M'_{\text{cut}} \approx 1.44 M_{\odot}$. Therefore, their 1D model missed the majority of the SLR yields attributed to our inner ejecta while giving very similar results for those attributed to our outer ejecta. In addition, the difference in the mass cut accounts for that in the ^{26}Al yield because $\approx 35\%$ of this yield is attributed to our inner ejecta.

As discussed in §4.2, our nominal ^{10}Be yield has large uncertainties due to the uncertain rate of $^{10}\text{Be}(p, \alpha)^7\text{Li}$ and possible effects of neutrino flavor oscillations (see Table 3). For completeness, we also explore the latter effects on the yields of the other SLRs. In the absence of flavor oscillations, we find that the yields of all SLRs from our adopted 1D model are close to those from our combined model. To estimate the effects of flavor oscillations, we use the 1D model to consider two extreme cases of either $\bar{\nu}_e \leftrightarrow \bar{\nu}_x$ or $\nu_e \leftrightarrow \nu_x$ oscillations as done for ^{10}Be . In either case, there is very little change to the yields of ^{53}Mn , ^{60}Fe , ^{107}Pd , ^{135}Cs , ^{182}Hf , and ^{205}Pb . For $\bar{\nu}_e \leftrightarrow \bar{\nu}_x$ oscillations, significant changes are a factor of ~ 2.3 increase in the ^{36}Cl yield due to the enhancement of $^{36}\text{Ar}(\bar{\nu}_e, e^+)^{36}\text{Cl}$ and a factor of ~ 1.4 increase in the

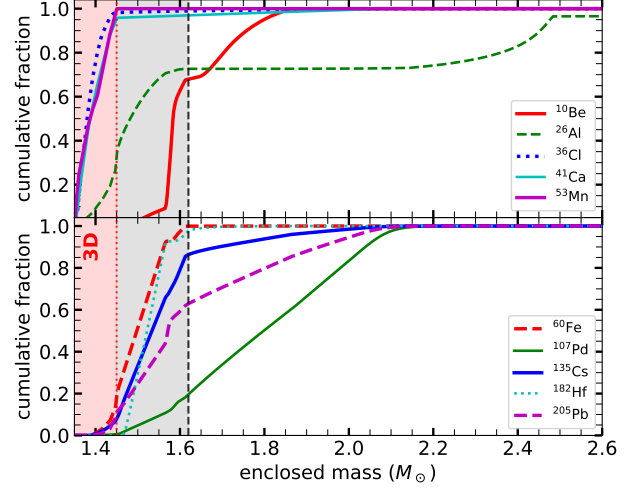


Figure 8. Cumulative fraction of the yield for each SLR as a function of the enclosed mass for our combined model. The dotted line at $M_{\text{tr}} = 1.45 M_{\odot}$ indicates the transition between the inner and outer ejecta. In a hypothetical scenario, the dashed line at $M_{\text{mix}} = 1.62 M_{\odot}$ represents the boundary inside which only a small fraction of the ejecta might have been injected into the proto-solar cloud.

^{41}Ca yield due to the enhancement of $^{41}\text{K}(\bar{\nu}_e, e^+)^{41}\text{Ca}$. For $\nu_e \leftrightarrow \nu_x$ oscillations, the only significant change is a factor of ~ 1.9 increase in the ^{26}Al yield due to the enhancement of $^{26}\text{Mg}(\nu_e, e^-)^{26}\text{Al}$.

Based on their yields, Banerjee et al. (2016) found that an $11.8 M_{\odot}$ CCSN could account for the abundances of ^{10}Be , ^{41}Ca , and ^{107}Pd in the ESS. For agreement with the data on ^{53}Mn , they proposed that only 1.5% of the innermost $\sim 0.01\text{--}0.12 M_{\odot}$ of the ejecta in their model might have been ejected due to fallback. In this scenario, however, the CCSN contribution to ^{60}Fe is only consistent with the values of $(^{60}\text{Fe}/^{56}\text{Fe})_{\text{ESS}} \sim (5\text{--}10) \times 10^{-7}$ reported by Mishra & Goswami (2014), which greatly exceed those of $(^{60}\text{Fe}/^{56}\text{Fe})_{\text{ESS}} = (1.01 \pm 0.27) \times 10^{-8}$ reported by Tang & Daughas (2015). Because neither our 3D simulation nor our 1D model shows any indication of fallback and our nucleosynthesis calculations give significantly different yields of ^{10}Be , ^{26}Al , ^{36}Cl , ^{41}Ca , and ^{53}Mn (see Table 4), below we re-examine the possible contributions from the $11.8 M_{\odot}$ CCSN to the SLRs in the ESS. We focus on our yields in Table 4 without considering neutrino flavor oscillations. Such considerations do not change our essential results, but will be commented on.

5.1. Implications for the ESS: Uniform Injection

Assuming that only the $11.8 M_{\odot}$ CCSN contributed a radioactive isotope R with mass number A_R and lifetime τ_R and that long-term production by other sources provided its stable reference isotope I with mass number A_I to the proto-solar

Table 4. Yields of SLRs and implications for the ESS

R/I	$Y_R (M_{\odot})$		τ_R (Myr)	$X_{I,\odot}$	Data	$(N_R/N_I)_{\text{ESS}}$	
	This Work	Banerjee et al. 2016				Uniform Injection	Tiered Injection
$^{10}\text{Be}/^9\text{Be}$	6.08×10^{-11}	3.26×10^{-10}	2.00	1.40×10^{-10}	$(7.5 \pm 2.5) \times 10^{-4}$	9.08×10^{-7}	5.38×10^{-5}
$^{26}\text{Al}/^{27}\text{Al}$	6.18×10^{-6}	2.91×10^{-6}	1.03	5.65×10^{-5}	$(5.23 \pm 0.13) \times 10^{-5}$	1.92×10^{-7}	7.94×10^{-6}
$^{36}\text{Cl}/^{35}\text{Cl}$	3.26×10^{-6}	1.44×10^{-7}	0.434	3.50×10^{-6}	$\sim (3-20) \times 10^{-6}$	6.22×10^{-7}	1.02×10^{-6}
$^{41}\text{Ca}/^{40}\text{Ca}$	7.11×10^{-6}	3.66×10^{-7}	0.147	5.88×10^{-5}	$(4.1 \pm 2.0) \times 10^{-9}$	3.89×10^{-9}	3.07×10^{-9}
$^{53}\text{Mn}/^{55}\text{Mn}$	2.73×10^{-5}	1.22×10^{-5}	5.40	1.29×10^{-5}	$(6.28 \pm 0.66) \times 10^{-6}$	6.30×10^{-6}	6.42×10^{-6}
$^{60}\text{Fe}/^{56}\text{Fe}$	4.17×10^{-6}	3.08×10^{-6}	3.78	1.12×10^{-3}	$(1.01 \pm 0.27) \times 10^{-8}$	9.42×10^{-9}	1.06×10^{-8}
$^{107}\text{Pd}/^{108}\text{Pd}$	1.42×10^{-10}	1.37×10^{-10}	9.38	9.92×10^{-10}	$(5.9 \pm 2.2) \times 10^{-5}$	4.39×10^{-7}	7.34×10^{-5}
$^{135}\text{Cs}/^{133}\text{Cs}$	3.06×10^{-10}	2.56×10^{-10}	3.32	1.24×10^{-9}	$\sim 5 \times 10^{-4}$	6.44×10^{-7}	1.76×10^{-5}
$^{182}\text{Hf}/^{180}\text{Hf}$	9.46×10^{-12}	8.84×10^{-12}	12.84	2.52×10^{-10}	$(9.72 \pm 0.44) \times 10^{-5}$	1.15×10^{-7}	7.22×10^{-7}
$^{205}\text{Pb}/^{204}\text{Pb}$	1.01×10^{-10}	9.20×10^{-11}	24.96	3.47×10^{-10}	$\sim 10^{-4}; 10^{-3}$	9.19×10^{-7}	7.30×10^{-5}

NOTE—Data references are: ^{10}Be (McKeegan et al. 2000; MacPherson et al. 2003; Wielandt et al. 2012; Srinivasan & Chaussidon 2013), ^{26}Al (Lee et al. 1976; Jacobsen et al. 2008), ^{36}Cl (Lin et al. 2005; Hsu et al. 2006; Jacobsen et al. 2011), ^{41}Ca (Ito et al. 2006; Liu et al. 2012), ^{53}Mn (Trinquier et al. 2008), ^{60}Fe (Tang & Dauphas 2015), ^{107}Pd (Schönbächler et al. 2008), ^{135}Cs (Hidaka et al. 2001), ^{182}Hf (Burkhardt et al. 2008), ^{205}Pb (Nielsen et al. 2006; Baker et al. 2010). Our yield of ^{10}Be has large uncertainties (see §4.2). The yields of ^{182}Hf assume the stellar decay rate of ^{181}Hf . Using the laboratory rate, Banerjee et al. (2016) obtained a higher yield of $4.04 \times 10^{-11} M_{\odot}$.

cloud, we calculate the number ratio of R to I in the ESS as

$$\left(\frac{N_R}{N_I}\right)_{\text{ESS}} = \frac{f Y_R / A_R}{X_{I,\odot} M_{\odot} / A_I} \exp(-\Delta / \tau_R), \quad (10)$$

where Y_R is the CCSN yield of R , $X_{I,\odot}$ is the solar mass fraction of I , f is the fraction of the R yield injected into the proto-solar cloud, and Δ is the interval between the production of R by the CCSN and its incorporation into ESS solids.

It is reasonable to assume that Δ is the same for all of the SLRs. We first consider the uniform injection scenario where they also have the same f . We search for f and Δ with which the results from Equation (10) can account for the data on some of the SLRs without exceeding those on the rest. As shown in Figure 9 and Table 4, for the “best-fit” values of $f = 3.26 \times 10^{-6}$ and $\Delta = 0.675$ Myr, the $11.8 M_{\odot}$ CCSN can account for the data on ^{41}Ca , ^{53}Mn , and ^{60}Fe while making negligible contributions to the other SLRs. Note that we have adopted the low values of $(^{60}\text{Fe}/^{56}\text{Fe})_{\text{ESS}} = (1.01 \pm 0.27) \times 10^{-8}$ reported by Tang & Dauphas (2015), which appear to be supported by the recent study of Trappitsch et al. (2018). Note also that simultaneous agreement with the data on ^{53}Mn and ^{60}Fe can be obtained for a relatively narrow range of f but a wide range of Δ . Effectively, this agreement determines the best-fit value of f while the additional agreement with the data on the very short-lived ^{41}Ca determines the best-fit value of Δ . Because neutrino flavor oscillations have little impact on the yields of ^{53}Mn and ^{60}Fe and only a modest effect (a factor of ~ 1.4) on the ^{41}Ca yield, they do not affect the above results significantly.

5.2. Implications for the ESS: Tiered Injection

The uniform injection scenario is commonly assumed in discussing the contributions from a CCSN to the SLRs in

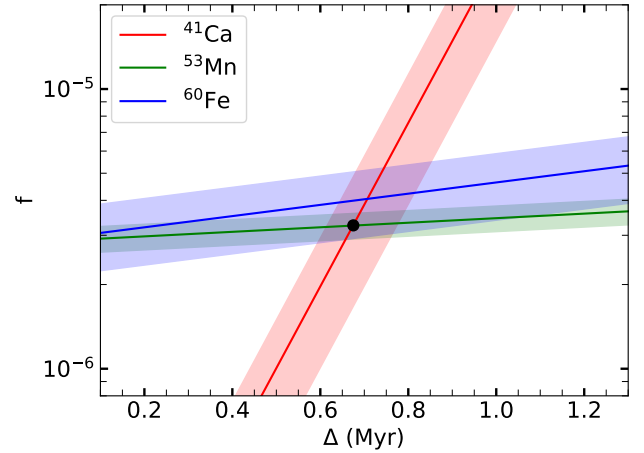


Figure 9. Determination of f and Δ for the uniform injection scenario. The band for an SLR shows combinations of f and Δ that allow the result from Equation (10) to account for the corresponding data. The black dot indicates the “best-fit” values of $f = 3.26 \times 10^{-6}$ and $\Delta = 0.675$ Myr, for which simultaneous agreement with the data on ^{41}Ca , ^{53}Mn , and ^{60}Fe can be obtained.

the ESS. This scenario appears to be supported by the simulations of Boss & Foster (1998), who found that material lagging far behind but moving with a similar velocity to the shock can be injected into a proto-stellar cloud with a similar efficiency to the material in the shock front. This result, however, applies only to the lagging material that can move to the shock-cloud interface when injection is still occurring through the Rayleigh-Taylor-like clumps. Simulations by Thornton et al. (1998) showed that in addition to a forward shock, there is also a reverse shock during the evolution of a CCSN remnant. This feature leads to a complicated

velocity profile, sometimes including negative velocities, for the material behind the forward shock. In view of such complications, we also consider a tiered injection scenario with a hypothetical boundary at the enclosed mass of M_{mix} for the CCSN ejecta. In this scenario, only a small fraction ϵ of the ejecta inside the boundary is mixed with the outside ejecta and injected into the proto-solar cloud with the same efficiency. Effectively, a fraction f of the yield in the outside ejecta is injected for each SLR, while the injected fraction for the inside ejecta is ϵf .

As an example, we choose $M_{\text{mix}} = 1.62 M_{\odot}$, $\epsilon = 0.5\%$, $f = 7 \times 10^{-4}$, and $\Delta = 1$ Myr. With these parameters, we can match the data on ^{41}Ca , ^{53}Mn , ^{60}Fe , and ^{107}Pd without exceeding those on the other SLRs (see Table 4). This result is not affected by neutrino flavor oscillations. We have also checked that the large uncertainties in the ^{10}Be yield would allow the highest possible value of $(^{10}\text{Be}/^9\text{Be})_{\text{ESS}}$ to be $\approx 2 \times 10^{-4}$, which is still a factor of ≈ 2.5 below the lower end of the observed values. Overall, the above result is close to what [Banerjee et al. \(2016\)](#) tried to achieve with similar values of f and Δ but by invoking fallback that we do not find in our 3D simulation or 1D model. Note also that our ^{41}Ca yield is ≈ 19 times higher than theirs and we have adopted the much lower values of [Tang & Dauphas \(2015\)](#) for the data on ^{60}Fe .

6. DISCUSSION AND CONCLUSIONS

We have studied the nucleosynthesis of an $11.8 M_{\odot}$ CCSN based on a 3D simulation of the inner ejecta. Accounting for the uncertainties in the neutrino transport with reasonable corrections to the neutrino emission properties, we have found mostly proton-rich inner ejecta that provide substantial yields of ^{45}Sc and ^{64}Zn . A proper assessment of the production of heavier isotopes, however, requires improvement of our simulation by incorporating more accurate neutrino transport to determine self-consistently the Y_e of the neutrino-heated ejecta. Combining the results for the inner ejecta with those for the outer ejecta from a suitable 1D model, we illustrate a method to obtain complete CCSN yields from a 3D simulation that only covers a limited central region. Such yields are important for chemical evolution considerations and for comparison to observational signatures such as the abundances of SLRs in the ESS.

Using our yields of the SLRs, we have explored the possibility that an $11.8 M_{\odot}$ CCSN might have triggered the formation of the solar system and provided some of the SLRs

in the ESS. In particular, we have discussed the uniform injection scenario, which can account for the data on ^{41}Ca , ^{53}Mn , and ^{60}Fe without exceeding those on the other SLRs, and the tiered injection scenario, which can account for the data on one more SLR, ^{107}Pd . The latter scenario is close to what [Banerjee et al. \(2016\)](#) tried to achieve. Our 3D simulation and 1D model, however, show no indication of the fallback that they invoked. Compared to their study, we have also identified large uncertainties in the production of ^{10}Be , obtained significantly larger yields of ^{26}Al , ^{36}Cl , ^{41}Ca , and ^{53}Mn , and adopted the much lower values of [Tang & Dauphas \(2015\)](#) for the data on ^{60}Fe , which appear to be supported by the more recent study of [Trappitsch et al. \(2018\)](#).

Finally, we emphasize that whereas our tiered injection scenario superficially looks like the usual scenario of mixing and fallback of the innermost CCSN matter (e.g., [Takigawa et al. 2008](#); [Banerjee et al. 2016](#)), the underlying physics and processes are very different. The usual scenario is closely related to the explosion mechanism that determines the mass cut and hence the actual amount of the ejecta, which are then injected into the proto-solar cloud with the same efficiency as in our uniform injection scenario. In contrast, our tiered injection scenario is motivated by the velocity profile during the CCSN remnant evolution, which could allow the inner part of the ejecta to be injected into the proto-solar cloud with a much lower efficiency than the outer part. Of course, the applicable scenario must ultimately be determined by detailed simulations of the CCSN and its subsequent interaction with the ISM including the proto-solar cloud. Analyses like those presented here need to be supported by such studies to test any candidate CCSN model as a trigger for the formation of the solar system.

This work was supported in part by the US Department of Energy [DE-FG02-87ER40328 (UM)]. BM was supported by ARC Future Fellowship FT160100035. This research was undertaken with the assistance of resources and services from the National Computational Infrastructure (NCI), which is supported by the Australian Government. It was supported by resources provided by the Pawsey Supercomputing Centre with funding from the Australian Government and the Government of Western Australia. Further calculations were run at the GSI Helmholtz Centre for Heavy Ion Research and Minnesota Supercomputing Institute. Figures were prepared with the matplotlib package ([Hunter 2007](#)).

REFERENCES

- Asplund, M., Grevesse, N., Sauval, A. J., & Scott, P. 2009, *ARA&A*, 47, 481
- Audi, G., Kondev, F. G., Wang, M., Huang, W. J., & Naimi, S. 2017, *Chin. Phys.*, C41, 030001
- Baker, R. G. A., Schönabächler, M., Rehkämper, M., Williams, H. M., & Halliday, A. N. 2010, *Earth and Planetary Science Letters*, 291, 39

- Banerjee, P., Qian, Y.-Z., Heger, A., & Haxton, W. C. 2016, *Nature Communications*, 7, 13639
- Bliss, J., Arcones, A., & Qian, Y. Z. 2018, *ApJ*, 866, 105
- Boggs, S. E., Harrison, F. A., Miyasaka, H., et al. 2015, *Science*, 348, 670
- Boss, A. P., & Foster, P. N. 1998, *ApJL*, 494, L103
- Brown, M. A.-P., Dees, E. B., Adamek, E., et al. 2018, *PhRvC*, 97, 035505
- Bruenn, S. W. 1985, *ApJS*, 58, 771
- Burkhardt, C., Kleine, T., Bourdon, B., et al. 2008, *GeoCoA*, 72, 6177
- Burrows, A., Radice, D., Vartanyan, D., et al. 2020, *MNRAS*, 491, 2715
- Cyburt, R. H., Amthor, A. M., Ferguson, R., et al. 2010, *ApJS*, 189, 240
- Ebinger, K., Curtis, S., Fröhlich, C., et al. 2019, *ApJ*, 870, 1
- Eichler, M., Nakamura, K., Takiwaki, T., et al. 2018, *Journal of Physics G Nuclear Physics*, 45, 014001
- Ertl, T., Janka, H.-T., Woosley, S. E., Sukhbold, T., & Ugliano, M. 2016, *ApJ*, 818, 124
- Ezzeddine, R., Frebel, A., Roederer, I. U., et al. 2019, *ApJ*, 876, 97
- Fröhlich, C., Hauser, P., Liebendörfer, M., et al. 2006, *ApJ*, 637, 415
- Glas, R., Just, O., Janka, H.-T., & Obergaulinger, M. 2018, *ArXiv e-prints*, arXiv:1809.10146
- Grebenev, S. A., Lutovinov, A. A., Tsygankov, S. S., & Winkler, C. 2012, *Nature*, 490, 373
- Hamuy, M. 2003, *ApJ*, 582, 905
- Harris, J. A., Hix, W. R., Chertkow, M. A., et al. 2017, *ApJ*, 843, 2
- Heger, A., & Woosley, S. E. 2010, *ApJ*, 724, 341
- Hidaka, H., Ohta, Y., Yoneda, S., & DeLaeter, J. R. 2001, *Earth and Planetary Science Letters*, 193, 459
- Hoffman, R. D., Woosley, S. E., Fuller, G. M., & Meyer, B. S. 1996, *ApJ*, 460, 478
- Hoffman, R. D., Woosley, S. E., & Qian, Y. Z. 1997, *ApJ*, 482, 951
- Horowitz, C. J. 2002, *PhRvD*, 65, 043001
- Hsu, W., Guan, Y., Leshin, L. A., Ushikubo, T., & Wasserburg, G. J. 2006, *ApJ*, 640, 525
- Hunter, J. D. 2007, *Computing in Science & Engineering*, 9, 90
- Iliadis, C., Longland, R., Champagne, A. E., Coc, A., & Fitzgerald, R. 2010, *NuPhA*, 841, 31
- Ito, M., Nagasawa, H., & Yurimoto, H. 2006, *Meteoritics and Planetary Science*, 41, 1871
- Jacobsen, B., Yin, Q.-z., Moynier, F., et al. 2008, *Earth and Planetary Science Letters*, 272, 353
- Jacobsen, B., Matzel, J., Hutcheon, I. D., et al. 2011, *ApJL*, 731, L28
- Janka, H.-T., Melson, T., & Summa, A. 2016, *ARNPS*, 66, 341
- Keil, M. T., Raffelt, G. G., & Janka, H.-T. 2003, *ApJ*, 590, 971
- Langanke, K., & Martínez-Pinedo, G. 2001, *Atomic Data and Nuclear Data Tables*, 79, 1
- Lee, T., Papanastassiou, D. A., & Wasserburg, G. J. 1976, *Geophys. Res. Lett.*, 3, 109
- Lentz, E. J., Bruenn, S. W., Hix, W. R., et al. 2015, *ApJL*, 807, L31
- Limongi, M., & Chieffi, A. 2018, *ApJS*, 237, 13
- Lin, Y., Guan, Y., Leshin, L. A., Ouyang, Z., & Wang, D. 2005, *Proceedings of the National Academy of Science*, 102, 1306
- Liu, M.-C., Chaussidon, M., Srinivasan, G., & McKeegan, K. D. 2012, *ApJ*, 761, 137
- MacPherson, G. J., Huss, G. R., & Davis, A. M. 2003, *GeoCoA*, 67, 3165
- McKeegan, K. D., Chaussidon, M., & Robert, F. 2000, *Science*, 289, 1334
- Mishra, R. K., & Goswami, J. N. 2014, *GeoCoA*, 132, 440
- Möller, P., Pfeiffer, B., & Kratz, K.-L. 2003, *PhRvC*, 67, 055802
- Müller, B. 2015, *MNRAS*, 453, 287
- . 2016, *PASA*, 33, e048
- Müller, B. 2019, *Annual Review of Nuclear and Particle Science*, 69, null
- Müller, B., Heger, A., Liptai, D., & Cameron, J. B. 2016, *MNRAS*, 460, 742
- Müller, B., & Janka, H. T. 2015, *MNRAS*, 448, 2141
- Müller, B., Janka, H.-T., & Marek, A. 2012, *ApJ*, 756, 84
- Müller, B., Tauris, T. M., Heger, A., et al. 2019, *MNRAS*, 484, 3307
- Müller, T., Prieto, J. L., Pejcha, O., & Clocchiatti, A. 2017, *ApJ*, 841, 127
- Nielsen, S. G., Rehkämper, M., & Halliday, A. N. 2006, *GeoCoA*, 70, 2643
- Ning, H., Qian, Y. Z., & Meyer, B. S. 2007, *ApJ*, 667, L159
- Nomoto, K., Kobayashi, C., & Tominaga, N. 2013, *ARA&A*, 51, 457
- O'Connor, E. P., & Couch, S. M. 2018, *ApJ*, 854, 63
- Pejcha, O., & Prieto, J. L. 2015, *ApJ*, 806, 225
- Pruet, J., Woosley, S. E., Buras, R., Janka, H. T., & Hoffman, R. D. 2005, *ApJ*, 623, 325
- Qian, Y. Z., & Woosley, S. E. 1996, *ApJ*, 471, 331
- Roberts, L. F., Woosley, S. E., & Hoffman, R. D. 2010, *ApJ*, 722, 954
- Schönbachler, M., Carlson, R. W., Horan, M. F., Mock, T. D., & Hauri, E. H. 2008, *GeoCoA*, 72, 5330
- Seitenzahl, I. R., Timmes, F. X., & Magkotsios, G. 2014, *ApJ*, 792, 10
- Sieverding, A., Langanke, K., Martínez-Pinedo, G., et al. 2019, *ApJ*, 876, 151
- Sieverding, A., Martínez-Pinedo, G., Huther, L., Langanke, K., & Heger, A. 2018, *ApJ*, 865, 143
- Srinivasan, G., & Chaussidon, M. 2013, *Earth and Planetary Science Letters*, 374, 11

- Sukhbold, T., Ertl, T., Woosley, S. E., Brown, J. M., & Janka, H.-T. 2016, *ApJ*, 821, 38
- Takigawa, A., Miki, J., Tachibana, S., et al. 2008, *ApJ*, 688, 1382
- Tamborra, I., Müller, B., Hüdepohl, L., Janka, H.-T., & Raffelt, G. 2012, *PhRvC*, 86, 125031
- Tang, H., & Dauphas, N. 2015, *ApJ*, 802, 22
- Thielemann, F.-K., Nomoto, K., & Hashimoto, M.-A. 1996, *ApJ*, 460, 408
- Thornton, K., Gaudlitz, M., Janka, H. T., & Steinmetz, M. 1998, *ApJ*, 500, 95
- Trappitsch, R., Boehnke, P., Stephan, T., et al. 2018, *ApJL*, 857, L15
- Trinquier, A., Birck, J. L., Allègre, C. J., Göpel, C., & Ulfbeck, D. 2008, *GeoCoA*, 72, 5146
- Vartanyan, D., Burrows, A., Radice, D., Skinner, M. A., & Dolence, J. 2019, *MNRAS*, 482, 351
- Wagoner, R. V. 1969, *ApJS*, 18, 247
- Wanajo, S., Müller, B., Janka, H.-T., & Heger, A. 2018, *ApJ*, 852, 40
- Weaver, T. A., Zimmerman, G. B., & Woosley, S. E. 1978, *ApJ*, 225, 1021
- Wielandt, D., Nagashima, K., Krot, A. N., et al. 2012, *ApJL*, 748, L25
- Woosley, S. E., Heger, A., & Weaver, T. A. 2002, *Reviews of Modern Physics*, 74, 1015
- Woosley, S. E., & Hoffman, R. D. 1992, *ApJ*, 395, 202
- Wu, M.-R., Qian, Y.-Z., Martínez-Pinedo, G., Fischer, T., & Huther, L. 2015, *PhRvC*, 91, 065016
- Yoshida, T., Kajino, T., Yokomakura, H., et al. 2006, *PhRvL*, 96, 091101
- Yoshida, T., Suzuki, T., Chiba, S., et al. 2008, *ApJ*, 686, 448
- Young, P. A., & Fryer, C. L. 2007, *ApJ*, 664, 1033